NDT and E International 102 (2019) 96–103

Contents lists available at ScienceDirect

NDT and E International

journal homepage: www.elsevier.com/locate/ndteint

Performance analysis of single-frequency near electrical resonance signal enhancement (SF-NERSE) defect detection

R.R. Hughes[a,*], S. Dixon[b]

[a] Mechanical Engineering, University of Bristol, Bristol, BS8 1TR, UK
[b] Department of Physics & School of Engineering, University of Warwick, Coventry, CV4 7AL, UK

ARTICLE INFO

Keywords:
Non-destructive testing
Non-destructive evaluation
NDE
NDT
Eddy-current
ECT
NERSE
Resonance
Titanium
Superalloys
PoD
Crack detection

ABSTRACT

In the search for ever more sensitive non-destructive testing (NDT) techniques to detect progressively smaller defects in increasingly complex industrial materials, environments and geometries, conventional eddy-current testing (ECT) methods, have reached their sensitivity limit. Fortunately, advanced resonance-based techniques, demonstrated in recent years, promise to help extend that limit, but, before such techniques can be implemented with confidence, a detailed understanding of their sensitivity and stability must be achieved. In this study, statistical probability-of-detection (PoD) analysis was performed to assess the sensitivity of a novel single-frequency, near electrical resonance signal enhancement (SF-NERSE) technique relative to an equivalent conventional probe operation. This study was performed on 36 real fatigue defects in Titanium 6V-4Al (Ti6-4) with defects ranging from 0.10 – 6.48 mm in surface extent. In addition, a critical evaluation of background noise stability in the SF-NERSE technique (a common concern with NERSE-based methods) was also performed to establish the viability of such a technique in relation to industrial inspection and assessment criteria. The results of this study demonstrate a sensitivity enhancement of up to 20% for the SF-NERSE method over conventional operation and, through controls, confirmed that the effect is a result of the resonance-shifting phenomenon and not just an increase in operational frequency. In addition, an examination of background noise implies that a SF-NERSE method exhibits more stable background noise than conventional excitation. This study validates the SF-NERSE technique and methodology as a viable industrial inspection technique, able to significantly improve detection capabilities.

1. Introduction

The structural integrity of industrial components is paramount for ensuring safety. There is no better example of this than in modern air travel, where the failure to detect component damage can have a catastrophic economic and human cost [1]. This was demonstrated by the recent Southwest Airlines engine failure, reportedly caused by undetected metal fatigue, resulting in the loss of a fan blade mid-flight, and the subsequent fatality of a passenger [2]. Non-destructive testing (NDT) methods such as ultrasonic testing (UT) and eddy-current testing (ECT) are employed regularly to inspect components for damage. Driven by the desire for safer flights, longer component lifetimes and lighter aircraft, NDT researchers strive to detect ever smaller signs of damage.

ECT is one of the most sensitive inspection techniques for detecting surface defects, capable of detecting sub-mm defects in ideal conditions. In recent years these inspections have approached a fundamental limit in their sensitivity, based on the size of manufacturable sensors. This is compounded when inspecting aerospace superalloys, such as Titanium 6V-4Al (Ti6-4), often used in aerospace turbine blades, which exhibit low electrical conductivities and high coherent background noise, reducing defect detectability [23].

One approach to improving ECT sensitivity has been the development and analysis of multifrequency inspections utilising multi-tone, chirp and pulsed excitation approaches [3,4]. Other researchers have highlighted a phenomenon in ECT sensors where frequencies around electrical resonance exhibit enhanced sensitivity to material discontinuities relative to conventional sub-resonance frequencies [5–7]. Hughes et. al. [5] presented a chirp frequency measurement technique to exploit the phenomenon, coined near electrical resonance signal enhancement (NERSE). Additional investigations have confirmed the cause of the phenomenon as resonance shifting due to inductive changes, and demonstrated the resonance behaviour due to lift-off is characteristically different to that due to defects, paving the way for

* Corresponding author.
E-mail address: robert.hughes@bristol.ac.uk (R.R. Hughes).

https://doi.org/10.1016/j.ndteint.2018.11.008
Received 31 May 2018; Received in revised form 6 October 2018; Accepted 14 November 2018
Available online 19 November 2018
0963-8695/

lift-off invariant NERSE inspections [8]. This exciting area of development has generated great interest with research now being carried out into the implementation and modelling of resonance-based measurement technology for a range of applications [9–13].

However, a major road-block to the adoption of such techniques has been due to the expectation that the enhanced sensitivity of resonance to defects will likely be coupled with an equal sensitivity to background noise, making evaluation of decision thresholds problematic. Here, research is presented demonstrating and characterising the sensitivity and stability of a single frequency NERSE excitation method on real surface-breaking fatigue cracks in Ti6-4 in relation to conventional excitation methods. The technique is used to conduct a probability of detection (PoD) study on these defects to conclusively demonstrate and quantify the sensitivity enhancing effect and noise stability of the NERSE-based inspection method.

2. Theory

2.1. Eddy-current testing of aerospace superalloys

Aerospace superalloys such as Ti6-4, Inconel and Waspalloy have characteristically low electrical conductivities, $\sigma \simeq 0.1 - 1\ MS/m$ [14]. As such these materials are inspected at comparatively high frequencies, (1–3 MHz) to limit the induced currents in the material to a shallow surface layer, improving the sensor resolution to surface breaking defects [15]. This principle is governed by the electromagnetic skin-depth (or standard depth of penetration), δ, defined as,

$$\delta = \sqrt{\frac{2}{\sigma\mu\omega}}, \tag{1}$$

where μ is the magnetic permeability and $\omega = 2\pi f$ is the angular frequency of excitation [16–18]. Increasing the frequency helps to improve the sensitivity of ECT inspections to defects in these materials. However, superalloys can also exhibit electrical anisotropy in their crystal structure, leading to high levels of coherent background noise in ECT measurements, reducing the signal-to-noise ratio (SNR) of measured defects [19].

2.2. Near electrical resonance signal enhancement

NERSE is the phenomenon observed in ECT sensors where the signal-to-noise ratio (SNR) of a defect measurement is significantly higher in a band of frequencies around electrical resonance. These frequencies are conventionally avoided by probe manufacturers and operators, owing to the perceived unpredictable and unstable nature of electrical resonance. Conventional probe operating frequencies finish significantly short of the electrical resonance of a typical ECT probe as demonstrated by Fig. 1. Fig. 1 shows the electrical resonance of an ECT probe above Ti6-4 compared to the signal-to-noise ratio (SNR) in relation to frequency of the sensor to 3 different wire-cut slots. The unit dim., here denotes dimensionless quantities. Operation below resonance keeps the measurement safely within a regime where the sensitivity scales linearly with frequency due to the inductive reactance component of impedance (ωL).

Beyond resonance, the reactive component of the system is dominated by capacitive changes within the cable, such that successful measurements of the inductive changes in a material are difficult. Between the conventional limit and the electrical resonance of the system lies a region of probe sensitivity dominated by the effects of defect-induced resonance shifting [8], where significant SNR enhancement occurs. The bandwidth region will be dependent on the probe inductance, cable capacitance, test material and defect size.

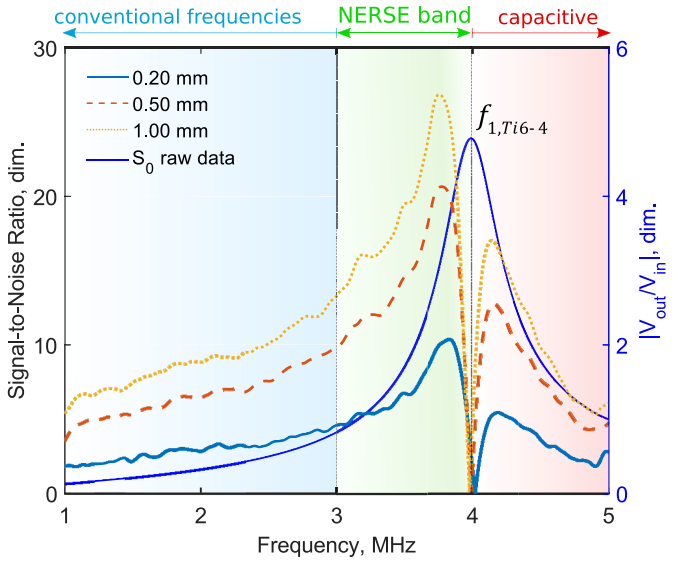

Fig. 1. Near Electrical Resonance Signal Enhancement (NERSE) signal-to-noise ratio (SNR) plot of signal magnitude (left-axis) for three discontinuities of varying depth in relation to electrical resonance on Ti6-4 (right-axis), after [20].

2.3. Sensitivity vs. stability

A technique could be very sensitive to defects whilst simultaneously being also very sensitive to background noise, resulting in highly unstable background noise levels. Although these levels, when averaged across a scan, might balance out, it poses a significant problem for inspectors using the technique when they come to define a detection (or decision) threshold.

Current industrial ECT protocols call for inspectors to set the decision threshold of an inspection to be 3 times the peak background noise level observed during a scan [21]. Should the defect be observed above this level (SNR > 3), then the part fails the inspection, but if a defect signal does not clear this threshold (i.e. SNR < 3) then the part is considered safe. This process is therefore greatly dependent on the *stability* of the background measurements.

The ideal inspection would be very sensitive to defects whilst exhibiting high background noise stability such that the decision threshold is not unnecessarily high based on anomalous noise readings.

3. Experimental method

An investigation was performed to investigate how operating at a single frequency, in the NERSE frequency band affects the inspection sensitivity and measurement stability of a ECT sensor. A series of PoD studies were carried out on 36 real fatigue cracks in Ti6-4 samples, operating the probe at a conventional operation frequency, within the NERSE frequency band, and at a control frequency in a higher resonance probe.

3.1. Experimental apparatus

ECT probes were driven using the experimental setup shown in Fig. 2. A Tektronix (Beaverton, Oregon, USA) 3021B arbitrary function generator was used to generate a voltage input function, V_{in}, signal which was converted into an equivalent drive current by an in-house built Howland current source. This current, I_{in}, is supplied via coaxial cable to the probe coil which is scanned across the surface of the test material on a xy-stage.

Constant, light pressure ensures the probe head is in contact with the material surface, and is achieved via a weighted probe holder. This

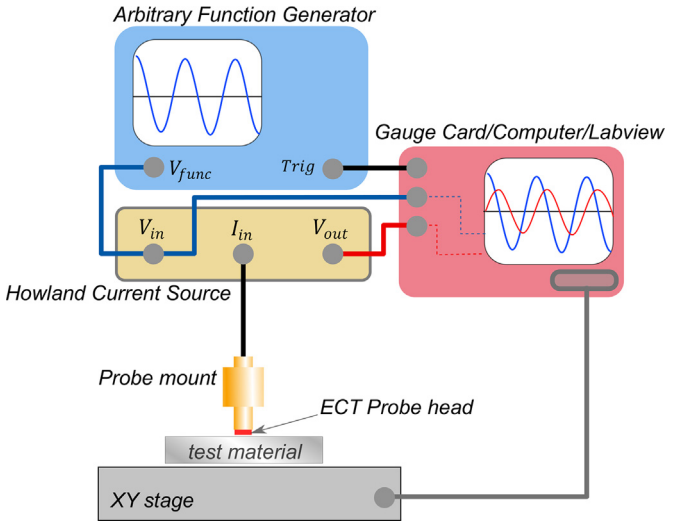

Fig. 2. Schematic diagram of the experimental set up for a 2D ECT scan. A Function generator outputs a voltage function which a Howland current source converts into an equivalent current function which is sent to the probe. The electrical properties of the probe are monitored via a Labview program as the probe is scanned across the surface of the test specimen.

allows the probe head to adapt to slight changes in the surface of the test material. The voltage in, V_{in}, and the voltage across the probe, V_{out}, were monitored and recorded using an analogue-to-digital (A/D) data acquisition card (digitisation rate of $20ns$) and custom Labview program.

Sinusoidal excitation frequencies were used to operate the ECT probe and the signals averaged over 1000 cycles to eliminate incoherent background noise. The time domain V_{in} and V_{out} waveforms were recorded, and analysed in the frequency domain to extract the complex impedance values.

3.1.1. Inspection coil

A sensor coil was manufactured in-house (see Fig. 3) to carry out the inspections. The critical properties of the probe are documented in Table 1.

The coil was operated using a 1.5 m long RG174, 50 Ohm coaxial cable (C_1). A calibration frequency sweep (see Ref. [5]) was carried out on a Ti6-4 defect calibration block, containing 3 wire-cut slots of varying depth, to determine where the NERSE frequency band was for the probe. The frequency spectrum of the probe (referred to as probe A) is shown in Fig. 4.

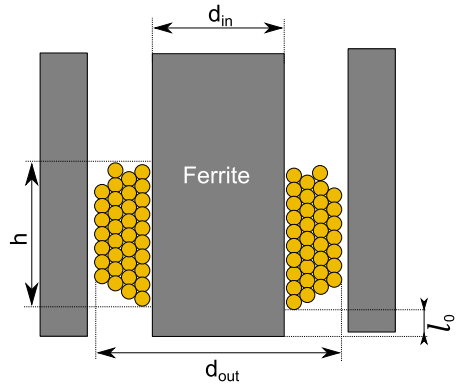

Fig. 3. Schematic diagram of the sensor.

Table 1
Physical and electrical properties of eddy-current probe.

Physical Properties	Value	Units
Number of turns, n	35	
Number of layers, N	4	
Wire diameter, t	0.10	mm
Core material	Ferrite 61[a]	
Core relative permeability, μ_r	35	
Core diameter, d_{in}	0.69 ± 0.01	mm
Coil outer diameter, d_{out}	1.14 ± 0.05	mm
Coil height, h	0.71 ± 0.01	mm
Inherent lift-off, l_0	0.34 ± 0.01	mm
Cable length, h	$1.50 \pm 0.01m$	m
Electrical Properties		
Coil inductance, L_L	8.77 ± 0.09	μH
Cable capacitance, C_c	158.4 ± 0.5	pF
Resonant frequency (air), f_0	4.27 ± 0.01	MHz

[a] From Fair-Rite Products Corp., Wallkill, NY, USA.

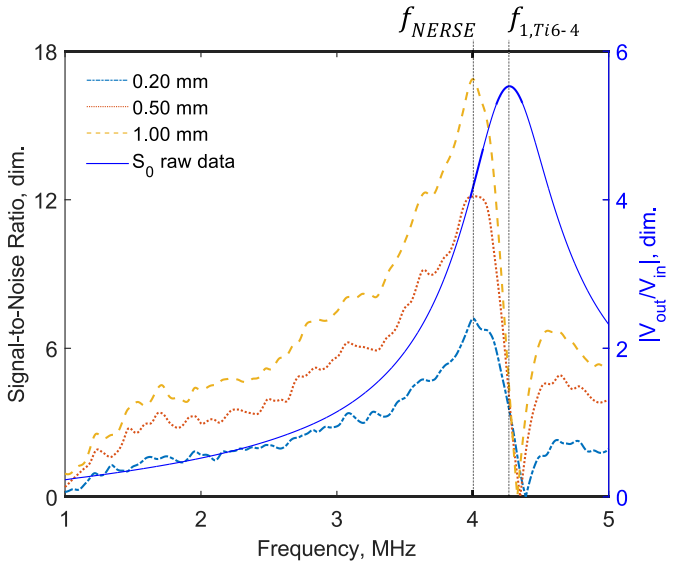

Fig. 4. Chirp excitation signal-to-noise 1–5 MHz frequency spectrum measurement of three calibration slots in Ti6-4 showing the electrical resonance of probe A on undamaged material, $f_{1,Ti6-4}$, and the peak NERSE frequency, f_{NERSE}.

3.2. Defects

A suite of 36 fatigue cracks in Ti6-4 bars, provided by Rolls-Royce plc., were used to carry out the PoD investigations. The cracks were generated by three-point bending technique, producing a range of crack ranging between $0.10 - 6.48mm$ in surface length, as measured using dye-penetrant testing (see acknowledgements). The specimens vary in surface condition, with surface roughnesses ranging from $0.15 - 1.25 \pm 0.05\mu m$, as measured by a Taylor Hobson (Leicester, UK) Surftronic 25 surface profiler.

3.3. Experimental procedure

A collection of 36 Ti6-4 fatigue test samples were scanned using three excitation methods to produce a distribution of ECT signals over a range of defect sizes for each method. Probability of detection (PoD) analysis was performed on each data set to achieve a direct comparison between standard ECT excitation and NERSE frequency measurements.

From the SNR spectrum in Fig. 4, two frequencies were selected at which to perform the PoD study using this probe setup (probe A). One inspection would be performed at a frequency representing the best conventional ECT excitation frequency (f_s = 3.25 MHz), and another

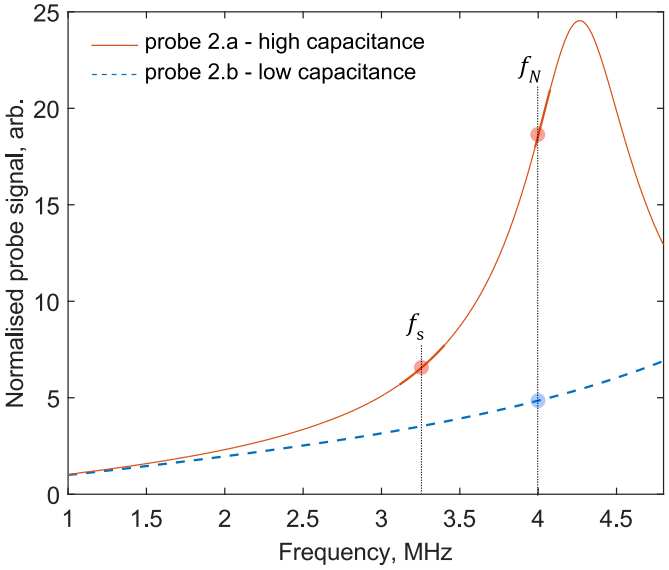

Fig. 5. Comparison of background frequency sweep signals of probe 2 connected with two different co-axial cable lengths (probe A and probe B) identifying the frequency of operation for the PoD studies.

PoD inspection would be carried out operating the probe at its peak NERSE frequency, $f_N = 4.0$ MHz.

A control study was also made to verify that the sensitivity improvement is merely a result of increasing the frequency of excitation and is not a result of the NERSE phenomenon. For this, the same coil (see Table 1) was operated using a shorter coaxial cable length of 0.25 m ($C_2 = 26.4 \pm 0.5\,pF$), reducing the capacitance of the system, such that the electrical resonance was at a significantly higher frequency. This coil-cable configuration, referred to from here on as probe B, was then used to perform another PoD study operating at f_N. Because of the higher resonant frequency this would be equivalent to operating within the conventional frequency range but would be subject to any beneficial material effects resulting from higher frequency operation (i.e. shallower shin-depth). The results of each of the studies are directly compared.

A swept frequency measurement for each of the probe configurations (probes A and B) on a section of undamaged Ti6-4 are compared in Fig. 5 to demonstrate the measurement frequencies relative to the frequency profiles of probes A & B.

Each PoD specimen was scanned point-by-point with a spatial resolution of $dx = dy = 0.25\,mm$ to replicate industrial inspection resolution. The capture depth of the measured signal was altered for the two different excitation frequencies so that 1000 cycles of the input frequency signal were captured, allowing a direct comparison between inspections (see Table 2).

The time-domain signals were Fourier transformed into the frequency domain and the ratio of $V_{out}(f)/V_{in}(f)$ calculated at the excitation frequency, for each point in the scan. The resulting C-scan data was then analysed to measure the defect signals.

Table 2
Time for 1000 cycles of excitation frequencies and capture depth of measurements.

f, MHz	Δt_{1000} ms	Sample Points
3.25	0.33	15385
4.00	0.25	12500

3.4. Data analysis method

For the purposes of this study, defect and noise signals were evaluated based on a phase-corrected peak amplitude analysis methodology detailed here-in. A combination of data processing steps were performed to analyse defect signals effectively. With reference to Fig. 6, the raw, complex C-scan data of size $m \times n$, $\tilde{A}_{mn}$, was analysed using the following procedure:

1. Balancing/Zeroing (background subtraction) - The average complex background signal, $\tilde{N}_0$, is calculated from an arbitrary area of the C-scan over a region of undamaged material (Fig. 6a). This value is then subtracted from every position in the C-scan to zero the scan data (Fig. 6b) as expressed by,

$$\tilde{B}_{mn} = \tilde{A}_{mn} - \tilde{N}_0. \tag{2}$$

2. *Complex Rotation* - The peak defect signal was located (white cross-hairs, Fig. 6b) and the complex value from that point, $\tilde{B}_{max}$, used in conjugate form to rotate all data-points in complex space via the equation,

$$\tilde{C}_{mn} = \frac{\tilde{B}_{mn}\tilde{B}^*_{max}}{|\tilde{B}_{max}|}. \tag{3}$$

The denominator in equation (3) ensures the overall magnitude of the complex data does not change. This process forces the peak defect signal to have zero phase i.e. to be entirely real (Fig. 6c).

3. *Median Filtering* - The real and imaginary components of the C-scan data are filtered using an inbuilt Matlab (MathWorks, Natick, Massachusetts, USA) median filter of pixel size 15×15, which is subtracted from the original data to remove any low spatial-frequency background variations from the image (Fig. 6d).
4. *Defect Measurement* - The maximum defect signal is selected within the real component C-scan image. The complex data for the pixels within a fixed cursor range (green cursor Fig. 6e) is displayed in a Lissajous (complex plane) plot in Fig. 6.f. The maximum real component amplitude for the defect signal is recorded.
5. *Background Noise Measurement* - The maximum real component amplitude from an arbitrary part of the undamaged material is then measured and recorded, in the same manor as the defect. One could use a background root mean squared average to calculate the background but this technique does not represent the maximum observable background signals. The arbitrary maximum approach used in this study is more representative of the potential for false calls within an industrial inspection.

The result of these processes is a phase invariant measurement of defect signal and background noise.

3.5. Probability of detection

PoD analysis was performed on the resultant measurement data sets, using statistical software package, R, implementing an industrially used extension, MIL-HDBK-1823, in accordance with RPS 906 [21]. In order to accurately assess the PoD of a given technique, suitable decision thresholds must be established.

3.5.1. Decision threshold a_{thresh}

Accurately defining the threshold level for a PoD analysis study is the most critical part of the statistical analysis. If the decision threshold, a_{thresh}, is underestimated, then the PoD analysis will calculate

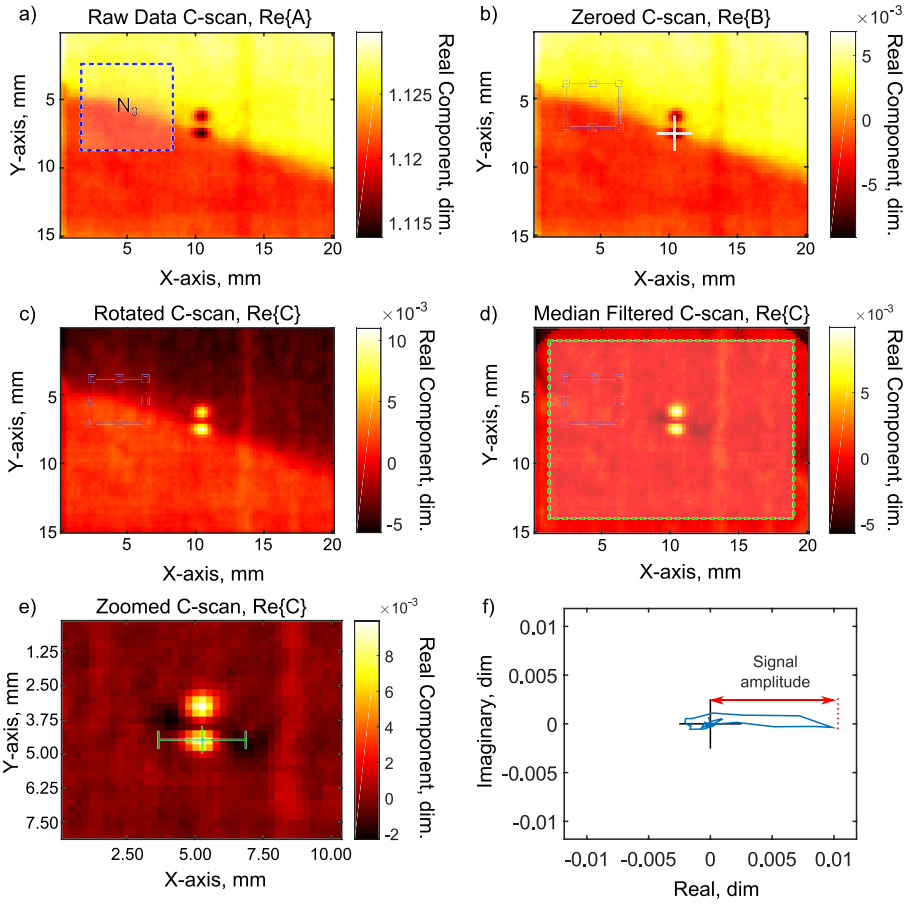

Fig. 6. Harmonic excitation data analysis process showing a C-scan of the real component at each stage.: a) Raw C-scan data showing arbitrary area of background material used to zero the image. b) Zeroed C-scan showing cross-hairs over the maximum defect signal pixel. The pixels complex value is used to rotate the complex C-scan data. c) Rotated C-scan. d) 15 × 15 pixel high-pass filtered C-scan. e) Zoomed in C-scan image showing measurement cursors over the peak defect signal and an arbitrary background point. And f) Lissajous (complex plane) plot showing the real vs imaginary components of the final C-scan data as measured along the x-axis of the green cursors in e) to give defect and noise indications. (For interpretation of the references to colour in this figure legend, the reader is referred to the Web version of this article.)

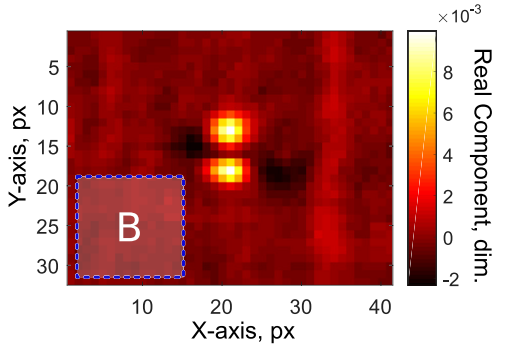

Fig. 7. Example arbitrary area of background material, *B*, used for background noise level measurements.

unrealistically high probe sensitivities. Overestimating a_{thresh} will lead to a sensitivity estimation lower than the real capability. The a_{thresh} level is typically set as 3 times the maximum background signal observed during inspection. This is to minimise the number of false calls. Two different approaches were used to set a_{thresh} and compared against one another.

The first approach took the maximum observed background noise signal, N_{max}, from the PoD study for each excitation technique, and used that value to set $a_{thresh,1} = 3N_{max}$. The second approach calculated the root mean squared (rms) average, N_{rms}, of all the noise signals recorded across the PoD study of a given inspection technique, and used that to set $a_{thresh,2} = 3N_{rms}$.

4. Results & discussion

Three independent inspection measurements were performed on 36 Ti6-4 fatigue crack samples using; probe A at its NERSE frequency ($f_{A:N}$ = 4.0 MHz) and at a standard excitation frequency below resonance, $f_{A:s}$ = 3.25 MHz. An additional control inspection was also performed using a higher resonant frequency probe (B) again at the frequency $f_{A:N}$ = 4.0 MHz. The data collected was used in two studies - The first was an assessment of measurement stability based on the variation of background noise in scans. The results of this study were then used to inform the a_{thresh} definitions in the second study - PoD analysis of each measurement approach.

4.1. Background noise stability

The stability of a measurement is just as important as the overall sensitivity. A measure of a technique's stability can be obtained via the analysis of the variation in background noise. To inform the definition of a_{thresh} in PoD analysis, a study was performed on the three different excitation approaches, using three different methods to analyse background noise. The three analysis methods were performed for each PoD sample, on an arbitrary area of undamaged material, e.g. *B* (Fig. 7). The background noise analysis methods were:

1. RMS Magnitude, $|B|_{rms}$ - Calculate the RMS average noise of all the absolute magnitudes of the background area data (phase insensitive averaged peak measurement). This gives the RMS average background signal regardless of it's orientation in phase space.
2. RMS Real Component, $\Re\{B\}_{rms}$ - Calculate the RMS average noise of all the real components of the background area data (phase sensitive averaged peak measurement). This gives the RMS average background noise signal observed in the same orientation as the defect signal.
3. Maximum Real Component, $\Re\{B\}_{max}$ - Measure the maximum real component noise from the background area (phase sensitive peak

Table 3
Probability of detection (PoD) study results showing the $a_{90/95}$ for the three measurement methods.

Probe	f, MHz	$a_{90/95}$ (mm)	
–	–	$(a_{thresh,1})$	$(a_{thresh,2})$
A	f_s = 3.25 MHz	0.86	0.40
A	f_{NERSE} = 4.0 MHz	0.72	0.32
B	f_c = 4.0 MHz	0.81	0.36

measurement). This gives the maximum background value observed in the same orientation as the defect signal.

The last method represents the method used in the PoD analysis to give the results shown in Fig. 10 and Table 3. Each of the three measurements listed above was performed on each PoD specimen. The noise data-sets were analysed to determine the percentage standard deviation of the methods for each inspection approach and noise measurement. The results, shown in Fig. 8.a, show that the maximum real component analysis, $\Re\{B\}_{max}$, has the maximum percentage variation compared to the other two methods. This demonstrates the inherent problems setting the decision threshold, a_{thresh}.

The $\Re\{B\}_{rms}$ provides the most stable measure of the three background signal measurements as expected given the averaging nature of the technique. However, this technique would not give as representative indication of maximum noise levels as the other methods. The results also show that the 4.0 MHz Control inspection exhibits the least variant background noise signals whereas the 3.25 MHz measurement consistently gives the highest variation compared to the other two inspections.

The results demonstrate that $\Re\{B\}_{rms}$ and $\Re\{B\}_{max}$ represent the most and least stable measures of background noise respectively. As such, the mean of each of these measurements will be used to set the decision thresholds in the PoD sensitivity analysis with $a_{thresh,1} = 3\bar{N}_{max}$ and $a_{thresh,2} = 3\bar{N}_{rms}$.

Fig. 8.b shows the overall noise distributions, across all (n = 36) PoD sample inspections, with respect to the mean rms and maximum noise measurements and the subsequent decision thresholds. The distributions shown represent all background noise regions (area B in Fig. 7) from all PoD scans taken and the mean $\Re\{B\}_{rms}$ ($\bar{N}_{rms}$) and $\Re\{B\}_{max}$ ($\bar{N}_{max}$) values are evaluated from this data and used in the PoD analysis below. Each distribution is scaled such that their centre and standard deviations align for direct comparison. All inspections exhibit comparable noise distributions.

4.2. Probability of detection sensitivity

The eddy-current signal responses of the three PoD inspection studies are shown in Fig. 9 (See Ref. [22] for a full description of the PoD analysis formula). PoD analysis was performed, using the two definitions for the decision threshold, a_{thresh}, detailed above. PoD analysis calculates the smallest statistically detectable defect length, $a_{90/95}$, following Annis 1999 [21].

The PoD curve for the NERSE excitation inspection with $a_{thresh,1} = 3\bar{N}_{max}$ is shown in Fig. 10. Plots for the other two inspection methods were omitted for the sake of concision. The $a_{90/95}$ results of the PoD analysis are summarised in Table 3.

The results displayed in Fig. 10 and Table 3 are a representative measure of the statistical sensitivity improvement that is achievable through operating ECT probes at frequencies within the NERSE band. The results demonstrate that operating at f_{NERSE} for a given sensor can reliably enhance the sensitivity to defects by $13-20\%$, relative to conventional inspection frequencies (f_s), and depending on the definition of a_{thresh}. The control study shows that a higher frequency excitation of 4.0 MHz will increase inspection sensitivity between $6-10\%$, relative to conventional inspection frequencies (f_s), and depending on the definition of a_{thresh}. However, in-spite of the increased noise stability observed in the 4.0 MHz control measurements (see Fig. 8.a), the results confirm the superior sensitivity enhancing effect achievable via NERSE-based excitation methods regardless of the method of setting the noise threshold.

4.2.1. Sizing uncertainty

One of the major uncertainties in this study is the accuracy of the crack sizing. The PoD cracks were sized using florescent dye penetrant inspection, but are therefore only a measure of the surface extent of the cracks. The actual geometry of the defects are unknown and this can therefore lead to anomalous results during ECT inspection. This is reflected by the results shown in Fig. 9.

5. Conclusions

A method for calibrating and performing single-frequency near electrical resonance signal enhancement (SF-NERSE) excitation of an ECT probe was demonstrated. A statistical PoD study demonstrated that SF-NERSE operation could increase the sensitivity of ECT inspections of fatigue cracks in Ti6-4 by up to 20% compared to typical industrial

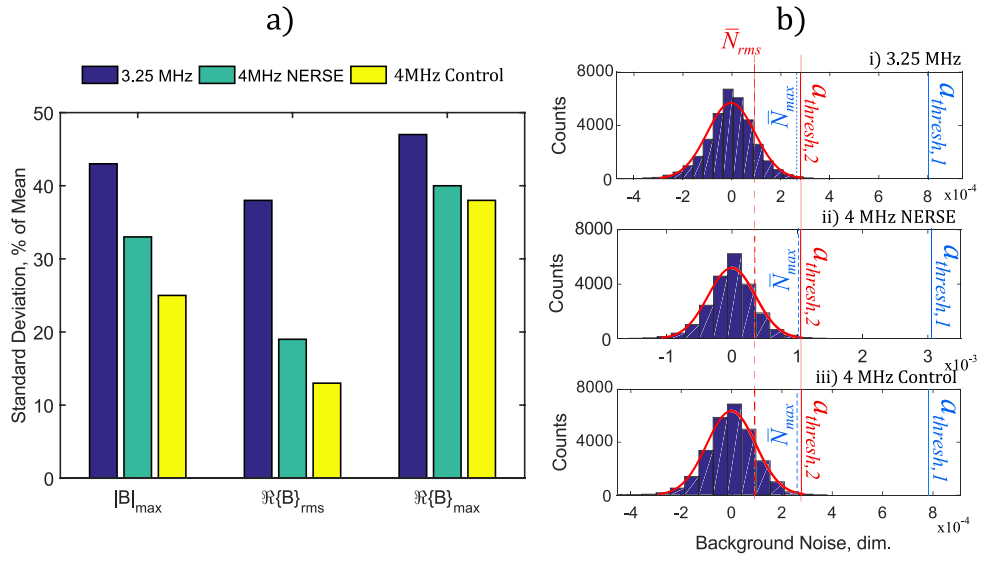

Fig. 8. Noise standard deviation (a) and distribution (b) across all PoD inspections (n = 36) for each different inspection technique: 3.25 MHz, 4.0 MHz NERSE and 4.0 MHz Control. Showing a) the percentage standard deviation of measured background values about the mean value (before background subtraction), for 3 measurement methods - $|B|_{rms}$, $\Re\{B\}_{rms}$ and $\Re\{B\}_{max}$, and b) the noise distributions (after background subtraction) for each measurement method relative to mean measured noise levels ($\bar{N}_{rms} = \overline{\Re\{B\}}_{rms}$ and $\bar{N}_{max} = \overline{\Re\{B\}}_{max}$) and subsequent (3N) decision thresholds.

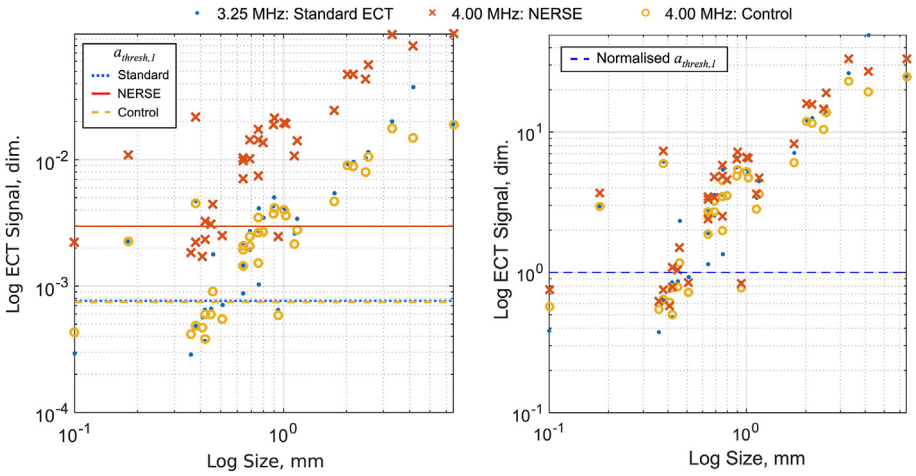

Fig. 9. Log-log plot of crack size verses signal response: (left) ECT crack signals, $\hat{a}$, for the 3 measurements along with their associated decision thresholds $a_{thresh,1}$ ($3\bar{N}_{max}$), and (right) $\hat{a}$ values normalised to the decision threshold to show direct comparison between all 3 measurement techniques.

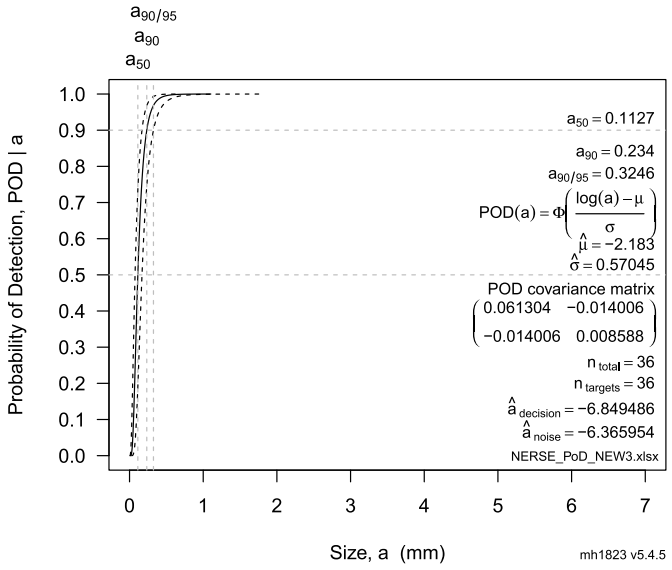

Fig. 10. Probability of detection curve for probe A operated at a frequency of 4.0 MHz (within the NERSE operating range for that setup).

excitation frequencies. This was confirmed, via control measurements, to be due to the NERSE phenomenon and not just the increase in frequency from 3.25 to 4.0 MHz.

The results also indicated that operating at SF-NERSE frequencies improved the stability of the background noise signals when compared to the standard operation frequency of 3.25 MHz. This result may be a feature of the specific coil geometry, design and frequencies examined. It is also possible that this is, in part, due to estimation error in the fft analysis, when the excitation frequency is not in a fractional ratio with the sampling frequency (see Table 2). Further studies are therefore required in order to verify if this effect is a general feature of operation at NERSE frequencies.

Regardless of the effect on background noise, operating within the NERSE band of an electrically resonating probe results in a significant sensitivity improvement to standard ECT probe geometries and designs. The effect can therefore be exploited to improve the detectable defect limit of inspections or be used to reliably detect smaller defects. The operational technique shown herein can be easily developed into an industrially applicable ECT system for single coil inspection. Continuing this work in conjunction with recent observations showing differences between resonance behaviour due to defects and lift-off, could allow lift-off variations to be accounted for in future developments, thereby allowing more robust NERSE measurement techniques. This can both improve confidence in industrial components and lead to greater part life-times and even allow redesigns to reduce component weight, resulting in lower manufacturing costs and more economic fuel efficiency.

Acknowledgements

The authors would like to thank the engineering and physical sciences research council (EPSRC) [grant number EP/F017332/1], Rolls-Royce plc. and the research centre for non-destructive evaluation (RCNDE) for supporting and funding the research detailed herein. The authors would also like to thank Rolls-Royce plc. for the use and characterisation of their PoD samples for this study. Data statement made below.

Appendix A. Supplementary data

Supplementary data to this article can be found online at https://doi.org/10.1016/j.ndteint.2018.11.008.

References

[1] Berger Joseph, Wilson Duff. Fatigue cracks caused hole in southwest jet. The New York Times; 2011 April 3, Available at: https://www.nytimes.com/2011/04/04/business/04plane.html, Accessed date: 25 May 2018.
[2] Jansen Bart. Southwest emergency landing: investigation focuses on broken fan. USA Today; 2018 April 18, Available at: https://eu.usatoday.com/story/news/2018/04/18/southwest-airlines-engine-failure- investigation/527498002/, Accessed date: 25 May 2018.
[3] Betta Giovanni, Ferrigno Luigi, Laracca Marco, Burrascano Pietro, Ricci Marco, Giuseppe Silipigni. An experimental comparison of multi-frequency and chirp excitations for eddy current testing on thin defects. Measurement 2015;63:207–20https://doi.org/10.1016/j.measurement.2014.12.015.
[4] He Yunze, Pan Mengchun, Luo Feilu, Tian Guiyun. Pulsed eddy current imaging and frequency spectrum analysis for hidden defect nondestructive testing and evaluation. NDT E Int 2011;44(4):344–52https://doi.org/10.1016/j.ndteint.2011.01.009.
[5] Hughes R, Fan Y, Dixon S. Near electrical resonance signal enhancement (NERSE) in eddy-current crack detection. NDT E Int 2014;66(0):82–9. https://doi.org/10.1016/j.ndteint.2014.04.009. ISSN 0963-8695.
[6] Hughes Robert, Dixon Steve. Eddy-current crack detection at frequencies approaching electrical resonance. Volume 1581 of *AIP conference proceedings* 2014. p. 1366–73. https://doi.org/10.1063/1.4864980.
[7] Liu Cunyue, Dong Yonggui. Resonant enhancement of a passive coil-capacitance loop in eddy current sensing path. Measurement 2012;45(3):622–6. https://doi.org/10.1016/j.measurement.2011.12.006.
[8] Hughes Robert R, Dixon Steve. Analysis of electrical resonance distortion for inductive sensing applications. IEEE Sensor J 2018;18(14). pages 1–1, 05.
[9] Meng Fanlin, Liu Xiucheng, Wang Heyun, He Cunfu, Wu Bin. Characterization of elastic and plastic behaviors in steel plate based on eddy current technique using a portable impedance analyzer. Journal of Sensors 2017;2017.
[10] Li Hor Yew, Zhong Yu, Bui Viet Phuong, Eng Png Ching. Electrical resonance eddy

current sensor for submillimeter defect detection vol. 10169. International Society for Optics and Photonics; apr 2017. p. 1016925. https://doi.org/10.1117/12.2260421.
[11] Kim Jong Min, Park Jae-Ha, Lee Ho Girl, Kim Hak-Joon, Song Sung-Jin, Chang-Sung Seok, Lee Young-Ze. An effective electrical resonance-based method to detect delamination in thermal barrier coating. J Therm Spray Technol 2018;27(3):336–43.
[12] Xu Xiaojuan, Ji Hongli, Qiu Jinhao, Cheng Jun, Wu Yipeng, Takagi Toshiyuki. Interlaminar contact resistivity and its influence on eddy currents in carbon fiber reinforced polymer laminates. NDT E Int 2018;94:79–91.
[13] Bui VP, Lane C, Zhong Y, Hor YL, Png CE. Model-assisted ndt for sub-mm surface-breaking crack detection in alloys. 2017 XXXIInd general assembly and scientific symposium of the international union of radio science URSI GASS); Aug 2017. p. 1–4. https://doi.org/10.23919/URSIGASS.2017.8105064.
[14] Kaye, Online Laby. Tables of physical & chemical constants. sixteenth ed. 1995 2005 2.6.1 - Electrical Resistivities, Available at: http://www.kayelaby.npl.co.uk/general_physics/2_6/2_6_1.html, Accessed date: 25 May 2018.
[15] Bassam A. Abu-Nabah and Peter B. Nagy. High-frequency eddy current conductivity spectroscopy for residual stress profiling in surface-treated nickel-base superalloys. NDT E Int, 40(5):405–418, doi: 10.1016/J.NDTEINT.2007.01.003.
[16] J Bowler and M Johnson. Pulsed eddy-current response to a conducting half-space. Magnetics, IEEE Transactions on, 33(3):2258–2264, doi: 10.1109/20.573841.
[17] Dodd CV, Deeds WE. Analytical solutions to eddy-current probe-coil problems. J Appl Phys 1968;39(6):2829–38.
[18] Smith Robert A, Hugo Geoffrey R, Harrison David J. Essential factors in improving the characterization of cracks and corrosion using transient eddy currents. Proc 6th joint FAA/NASA/DoD conf on aging aircraft, san francisco. 2002.
[19] Blodgett Mark, Hassan Waled, Peter B Nagy. Theoretical and experimental investigations of the lateral resolution of eddy current imaging. Mater Eval 2000;58(5):647–54.
[20] Hughes R, Dixon S. Near electrical resonance signal enhancement (NERSE) for sub-millimetre detection in aerospace superalloys. International Journal of Aerospace and Lightweight Structures (IJALS) 2014;4(2):107–20. https://doi.org/10.3850/S2010428615100096.
[21] Annis C. Nondestructive evaluation system reliability assessment. Department of Defence Military Handbook; 1999. 1823, MIL-HDBK-1.
[22] Hughes Robert Rhys. High-sensitivity eddy-current testing technology for defect detection in aerospace superalloys PhD thesis University of Warwick; 2015
[23] Blodgett M, Hassan W, Nagy PB. Theoretical and experimental investigations of the lateral resolution of eddy current imaging. Materials Evaluation 2000;58(5):647–54.